THE JOURNAL OF PHYSICAL CHEMISTRY C

Article

pubs.acs.org/JPCC

Influence of Tetrahedral Layer Charge on the Organization of Interlayer Water and Ions in Synthetic Na-Saturated Smectites

Baptiste Dazas,[*,†,‡] Bruno Lanson,[†,‡] Alfred Delville,[§] Jean-Louis Robert,[∥] Sridhar Komarneni,[⊥] Laurent J. Michot,[#,∇] and Eric Ferrage[¶]

[†]Univ. Grenoble Alpes, ISTerre, F-38000 Grenoble, France

[‡]CNRS, ISTerre, F-38000 Grenoble, France

[§]Université d'Orléans – CNRS, CRMD, F-45071 Orléans, France

[∥]IMPMC, Sorbonne Universités, UMR 7590, UPMC, CNRS, MNHN, IRD, 4 Place Jussieu, 75252 Paris Cedex 05, France

[⊥]Materials Research Institute, Penn State University, University Park, Pennsylvania 16802, United States

[#]Sorbonne Université, UPMC Univ. Paris 06, Phenix, F-75252 Paris, France

[∇]CNRS, Phenix, F-75252 Paris, France

[¶]Université de Poitiers – CNRS, IC2MP-HydrASA, F-86022 Poitiers, France

Supporting Information

ABSTRACT: Smectite hydration strongly influences dynamical properties of interlayer cations and thus the fate of H_2O and pollutants in surficial systems where smectite-based materials are often used as a major barrier component. Smectite crystal chemistry is known to rule its hydration, although the influence of specific parameters such as the amount and location of layer charge deficit remains poorly understood. A set of tetrahedrally charged trioctahedral smectites, with a common structural formula $^{inter}[Na_x]^{oct}[Mg_6]^{tet}[Si_{8.0-x}Al_x]O_{20}(OH,F)_4$ and a layer charge (x) varying from 0.8 to 3.0, were thus synthesized to assess the influence of layer charge on smectite hydration and interlayer structure. Both hydroxylated and fluorinated samples were synthesized because of the increasing use of the latter varieties in recent spectroscopic studies aiming at the determination of interlayer H_2O dynamical properties. The distribution of charge-compensating cations and of associated H_2O molecules was determined both experimentally from the modeling of X-ray diffraction patterns and numerically from Monte Carlo molecular simulations performed in the grand canonical ensemble. The consistency of both approaches for hydroxylated samples allowed gaining insights into the specific influence of smectite crystal chemistry. For a given hydration state, H_2O content is about constant in hydroxylated saponites, independent of layer charge, whereas smectite layer-to-layer distance decreases with increasing layer charge because of the enhanced cation-layer electrostatic attraction. As a result, positional disorder of interlayer H_2O molecules is reduced because of stronger steric constraints and of the increased density of electronegative sites at the surface of the clay layer. Fluorine-for-hydroxyl isomorphic substitutions likely increase further electronegativity of the clay layer surface leading to further reduction of the interlayer H_2O content and to the formation of Na^+ inner sphere complexes at the clay layer surface. When normalized to the number of interlayer cations, the number of interlayer H_2O molecules decreases with increasing layer charge, and the proportion of these H_2O molecules hydrating interlayer cations increases, thus increasing the stability of most hydrated states toward lower relative humidity conditions. Smectite hydration evolution appears as a steady process with no tendency to interlayer cation ordering at the smectite-to-vermiculite limit of ~1.3 charge per $O_{20}(OH,F)_4$.

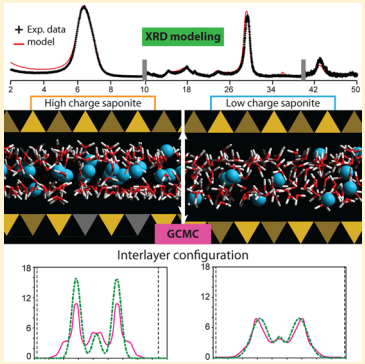

INTRODUCTION

Smectite represents the most hydrated pole of phyllosilicates and is used hereafter as a generic term for all expandable varieties thereof. Smectite TOT, or 2:1, layers include two tetrahedral sheets embedding an octahedral one. Isomorphic substitutions within both tetrahedral and octahedral sheets induce a permanent layer charge deficit, compensated for by the presence in the interlayer space of exchangeable cations whose hydration properties control smectite colloidal behavior and crystalline swelling.[1−7] The latter has been long described and is characterized by the stepwise expansion of the layer-to-layer distance with increasing water activity.[7−12] This behavior plays a pivotal role in the physical and chemical behaviors of surface environments and sedimentary rocks where smectite is found, frequently as a major mineral component.[13−22] More specifically, smectite hydration can strongly impact dynamical properties of interlayer cations and thus the transfer and fate of H_2O and pollutants[23−27] but also smectite ability to produce a variety of nanocomposites for different applications.[28−30]

Received: December 11, 2014
Revised: January 31, 2015
Published: February 2, 2015

DOI: 10.1021/jp5123322
J. Phys. Chem. C 2015, 119, 4158−4172

From the contrasting stability of the different smectite hydrates as a function of water activity, smectite crystal chemistry, and more especially the amount and location of smectite layer charge deficit, has long been known to exert a pivotal control on smectite hydration.[6,31−34] This influence allowed in particular the differentiation between smectite and vermiculite as a function of layer charge [0.6−1.2 and 1.2−1.8 e^- per $O_{20}(OH)_4$, respectively], owing to their contrasting capacity to incorporate polar molecules such as H_2O and ethylene glycol.[35−37] The amount of smectite layer charge is thus an essential parameter of smectite-rich bentonite deposits and is most often determined from the cation exchange capacity of the material.[38] Consistently, over the past decade or so significant efforts have been devoted to assess the results derived from a variety of chemical compositions and alkyl ammonium methods and to develop alternative methods aiming at a more precise and more reliable measurement of this parameter.[39−48]

The correlation between smectite crystal chemistry and hydration properties remained described essentially at the layer scale, however.[34,49−54] X-ray diffraction profile modeling allowed refining this description by taking hydration heterogeneity into account and provided, together with molecular modeling, a comprehensive picture of interlayer H_2O and cation configurations for the different smectite hydrates.[2,50,55−67] In particular, these publications confirm the distribution of interlayer H_2O molecules about one or two positions along the c^* axis (the "planes" of interlayer H_2O molecules) in mono- and bihydrated layers, respectively. Evolution of interlayer structure was not investigated systematically as a function of smectite crystal chemistry, however. Based mainly on the comparison between two samples with contrasting layer charge, previous reports indicate an increased stability of most hydrated hydration states with increasing layer charge.[50−52,67] In addition, the positional disorder about the "ideal" interlayer H_2O positions decreases with increasing layer charge, resulting in sharper electron density profiles associated with a stronger polarization of H_2O molecules.[50−52,67] This evolution, and more especially its steady or abrupt character, and a quantitative description of influential crystal and interaction parameters remain, however, key to deciphering and understanding the influence of smectite crystal chemistry on its hydration at a more relevant molecular scale.

In the present study, special attention was thus paid to assess the influence of the amount of layer charge on the hydration behavior of tetrahedrally substituted smectites. Interlayer H_2O contents were determined for smectites with a layer charge [per $O_{20}(OH)_4$] ranging from ∼0.8 (smectite *sensu stricto*) to 1.2−1.4 (vermiculite) and further to 2.0−3.0 (micas) using H_2O vapor (de)sorption isotherms. The distribution of both H_2O molecules and charge-compensating cations within the smectite interlayer was determined from X-ray diffraction profile modeling for both mono- and bihydrated layers. Finally, Monte Carlo simulations were performed in the grand canonical ensemble to elucidate the origin of the contrasting hydration behaviors determined for the different samples. The influence of F-for-OH anionic substitutions on smectite hydration was also assessed.

MATERIALS AND METHODS

Samples. Synthetic expandable phyllosilicates with a common structural formula $^{inter}[Na_x]^{oct}[Mg_6]^{tet}[Si_{8.0-x}Al_x]O_{20}(OH,F)_4$ and a layer charge (x) varying from 0.8 to 3.0 were used. These "saponites" are hereafter referred to as Sap-x-OH/F, with OH/F describing the prevailing structural anion. Hydration of Sap-0.8-OH and Sap-1.4-OH has been investigated previously.[50] Sap-1.0-OH, Sap-1.2-OH, and Sap-2.0-OH were synthesized hydrothermally from gel precursors in an externally heated Morey-type pressure vessel with an internal silver tubing,[68,69] as the previous two samples. Synthesis conditions were a temperature of 400 °C, a water pressure of 1 kbar, and a duration of 4 weeks. Two fluorinated saponites (Sap-1.0-F and Sap-3.0-F) were synthesized using kaolinite, silicic acid, or silica gel or amorphous silica, magnesium fluoride, and sodium chloride as detailed elsewhere.[70]

All samples were initially sodium-saturated at room temperature by contact with 1 mol·L^{-1} aqueous solutions of NaCl. Saponites were shaken mechanically in saline solutions for 24 h before separation of the solid fraction by centrifugation and addition of a fresh saline solution. Four repetitions of these steps ensured a complete cation exchange. Excess sodium chloride was then removed by rinsing the solid four times by immersion for 24 h in deionized water (Siemens UltraClear, 18.2 MΩ.cm^{-1}) and separation of the solid fraction by centrifugation.

Water Vapor Desorption Isotherms. Isotherms were measured with a lab-built quasi-equilibrium setup designed around a Setaram MTB 10-8 symmetrical microbalance.[71] Water vapor was supplied to the sample (kept at 30 °C) at a slow flow rate from a source at 45 °C to maintain quasi-equilibrium conditions at all times. Isotherms were deduced from the simultaneous measurements of mass uptake and equilibrium pressure (gauge 0−13.33 kPa). Samples (∼100 mg) were initially outgassed at 110 °C for 18 h under a residual pressure of 1 Pa. Additional sorption isotherms were collected volumetrically at 25 °C on Sap-1.0-F and Sap-3.0-F using a BELSORP-max instrument from BEL Japan. In this case, samples (∼200 mg) were initially outgassed at 150 °C for 24 h under a residual pressure of 10^{-5}−10^{-4} Pa.

X-ray Diffraction (XRD). For all samples, oriented slides were prepared by drying at room temperature an aqueous clay suspension on glass slides. XRD patterns were then recorded using a Bruker D8 diffractometer equipped with an MHG Messtechnik humidity controller coupled to an Anton Paar CHC+ chamber. Intensities were measured with a SolXE Si(Li) solid-state detector (Baltic Scientific Instruments) for 4 s per 0.04° 2θ step over the 2−50° 2θ Cu Kα angular range. Divergence slit, the two Soller slits, the antiscatter, and resolution slits were 0.3°, 2.3°, 0.3°, and 0.1°, respectively. Samples were kept at 23 °C in the CHC+ chamber during the whole data collection. Samples were kept also under a constant flow of mixed dry/saturated air to maintain the desired relative humidity (RH) after an initial equilibration at ∼97% RH. RH was continuously monitored with a hygrometer (uncertainty of ∼2% RH) located close to the sample.

The algorithms developed initially by Drits and co-workers were used to fit experimental XRD profiles over the recorded 2−50° 2θ Cu Kα angular range using a trial-and-error approach.[72,73] Instrumental and experimental factors such as horizontal and vertical beam divergences, goniometer radius, and length and thickness of the oriented slides were measured and introduced without further adjustment. The mass absorption coefficient (μ^*) was set to 45 cm^2 g^{-1}, as recommended by Moore and Reynolds.[62] Variable parameters included the layer-to-layer distance. The coherent scattering domain size along the c^* axis was characterized by a maximum value, set to 80 layers, and by a mean value (N). The z-coordinates of all atoms constituting the 2:1 (or TOT) smectite layer were set as proposed by Ferrage et al.[50]

DOI: 10.1021/jp5123322
J. Phys. Chem. C 2015, 119, 4158−4172

Table 1. Structural Parameters Used to Fit Experimental XRD Patterns of Sap-1.2-OH as a Function of Relative Humidity

relative humidity %		5	10	20	40	60	95
phase 1	ab. (%)				0.46	0.92	1.00
	0W						
	1W				0.40		
	2W				0.60	1.00	1.00
	CSD size[b]				8	12	12.5
phase 2	ab. (%)	0.10	0.08	0.06	0.41	0.08	
	0W	0.30					
	1W	0.70	0.80	0.80	0.70	0.50	
	2W		0.20	0.20	0.30	0.50	
	CSD size[b]	10	8	8	8	20	
phase 3	ab. (%)	0.90	0.92	0.94	0.13		
	0W						
	1W	1.00	1.00	1.00	0.90		
	2W				0.10		
	CSD size[b]	16	16	16	10		
number of H_2O molecules per $O_{20}(OH)_4$	1W	3.0	3.5	3.8	4.0	4.2	
	2W		8.5	8.5	8.6	9.0	9.7
Debye–Waller factor of interlayer species[a]	BWat1	50	50	50	50	20	20
	BWat2	30	30	30	30	10	10
	Bcat	5	5	5	5	5	5
layer-to-layer distance (Å)	0W	9.70	9.70	9.70	9.70	9.70	9.70
	1W	12.02	12.16	12.32	12.45	12.60	12.33
	2W		14.93	14.93	14.95	14.99	15.07
σz (Å)	0W	0.20	0.20	0.20	0.15	0.15	0.12
	1W	0.24	0.24	0.24	0.20	0.20	0.20
	2W	0.20	0.20	0.20	0.15	0.15	0.12
additional parameters	Δ2W (Å)	1.3	1.3	1.3	1.3	1.4	1.4
	σ^* (deg)	0.8	1.1	0.8	0.2	0.2	0.0

[a]Debye–Waller factor of interlayer H_2O is given in Å^2 for each layer type. [b]Average CSD size is given in layers per crystal.

The interlayer configuration used for bihydrated layers (2W, d_{001} = 14.9–15.7 Å) was that proposed initially by Ferrage et al. with one plane of H_2O molecules on each side of the interlayer midplane that hosts cations.[51] This model is characterized by the distance (Δd2W) between the interlayer midplane and each of the planes of H_2O molecules. For monohydrated layers (1W, d_{001} = 11.6–12.9 Å) both cations and H_2O molecules were located in the interlayer midplane. A similar configuration was used for dehydrated layers (0W, d_{001} = 9.7–10.2 Å), without interlayer H_2O molecules however. The overall interlayer water content at a given RH was constrained by water vapor sorption isotherms and was not considered as a variable parameter in the present work, although the distribution of this global content between the different types of hydrated layers was refined. N, Δd2W, and the Debye–Waller factor of H_2O molecules (B_{wat}) were considered also as variable parameters, the latter in an effort to optimize the electronic density profile of interlayer species as proposed by Dazas et al.[58] The fitting procedure is detailed elsewhere.[50−52] The unweighted R_p parameter, which is mainly influenced by fit quality of intense diffraction maxima, was used to quantify the overall fit quality.[74]

Grand Canonical Monte Carlo (GCMC) Simulations. Monte Carlo simulations were performed in the grand canonical ensemble to assess the content of interlayer H_2O and the equilibrium state of interlayer species (H_2O and cations) for hydroxylated samples.[75−77] Simulations were performed at both 20 and 90% RH and 300 K (1W and 2W hydration states, respectively). A homemade program was used for the simulation.[27,78−82] The rigid simulation box included three interlayers and related 2:1 layers. Each layer encompassed six and four unit cells along the a and b directions, respectively, with a $-a/3$ layer displacement leading to a face to face configuration for ditrigonal cavities. The chosen layer displacement allows matching closely H_2O contents determined experimentally,[50] whereas the actual value of this displacement does not influence significantly the distribution of interlayer species along the c^* axis (data not shown). The layer-to-layer distance was set from experimental d_{001} values (Tables 1 and 2)[50] or interpolated linearly when experimental value was lacking. $^{inter}[Na_x]^{oct}[Mg_6]^{tet}[Si_{8.0-x}Al_x]O_{20}(OH,F)_4$ compositions with x = 0.6, 0.8, 1.0, 1.1, 1.2, 1.4, and 2.0 were used. Al-for-Si substitutions were located randomly in each layer with an exclusion rule preventing two Al atoms from occupying neighboring tetrahedra. The ClayFF force field and SPC/E water model were selected to simulate the clay–water interactions,[83] as recommended by Ferrage et al. from the cross-validation of atomic density profiles derived from GCMC simulations and X-ray and neutron diffraction pattern modeling.[67] Lennard-Jones (LJ) potentials of interlayer cations derived by Aaqvist were used,[84] whereas the distance parameter R_0 of oxygen atoms from the 2:1 layer was increased from 3.55 to 3.80 Å.[67] For a given partial pressure, water chemical potential is given by the following relation

$$\frac{\mu}{kT} = \frac{\mu^0}{kT} + \ln\left(\frac{P}{P^0}\right) \quad (1)$$

with

$$\frac{\mu^0}{kT} = \ln(\Lambda^3 \times \rho) \quad (2)$$

DOI: 10.1021/jp5123322
J. Phys. Chem. C 2015, 119, 4158−4172

Table 2. Structural Parameters Used to Fit Experimental XRD Patterns of Sap-2.0-OH as a Function of Relative Humidity

relative humidity %		16	52	88
phase 1	ab. (%)	0.01	0.81	0.76
	0W			
	1W	0.81		
	2W	0.19	1.00	1.00
	CSD size	15	14.5	13.5
phase 2	ab. (%)	0.10	0.14	0.18
	0W	0.22		
	1W	0.78	0.30	0.30
	2W		0.70	0.70
	CSD size	20	10	10
phase 3	ab. (%)	0.85	0.03	0.05
	0W			
	1W	1.00	0.90	0.90
	2W		0.10	0.10
	CSD size	19	5	5
phase 4	ab. (%)	0.04	0.02	0.01
	0W	0.60	0.45	0.45
	1W	0.40	0.55	0.55
	2W			
	CSD size	25	30	30
number of H_2O molecules per $O_{20}(OH)_4$	1W	3.7	4.0	4.2
	2W	8.5	9.2	9.9
Debye–Waller factor of interlayer species	BWat1	25	50	50
	BWat2	7	7	7
	Bcat	5	5	6
layer-to-layer distance (Å)	0W	9.70	9.70	9.70
	1W	12.12	12.14	12.15
	2W	14.83	14.85	14.885
σz (Å)	0W/1W/2W	0.21	0.05	0.10
additional parameters	Δ2W (Å)	1.20	1.34	1.37
	σ^* (deg)	2.9	2.3	2.3

considering H_2O vapor as an ideal fluid, Λ being the H_2O de Broglie wavelength (0.238376 Å), k the Boltzmann constant, and ρ the vapor density at 300 K (7.7087481×10^{-7} molecules·Å^{-3}). GCMC simulations encompassed 6000 blocks, each with 10 000 elementary steps allowing stabilization of interlayer H_2O molecule content. At each step, one of the clay interlayers was selected randomly, and with an equal probability an attempt was made (i) to remove a H_2O molecule, (ii) to add a H_2O molecule in a random configuration, or (iii) to move a randomly chosen cation or H_2O molecule. During calculations, an Ewald summation was used in addition to the three-dimensional minimum image convention to ensure the convergence of the electrostatic energy.[85] A final run including 1000 blocks of 5000 steps was performed to generate the equilibrium properties of interlayer species and to derive three-dimensional radial cation–H_2O distribution functions.

RESULTS AND DISCUSSION

Water Vapor Desorption Isotherms. Isotherms obtained for hydroxylated samples are typical for sorption of polar molecules on swelling phyllosilicates,[86] the two steps corresponding to domains dominated by 2W and 1W smectite layers.[87] Capillary sorption of H_2O molecules when approaching water vapor saturation prevents determining the upper end of the 2W stability domain. On the other end, this domain extends down to ~60, ~50, and ~45% RH for Sap-0.8-OH, Sap-1.0-OH, and Sap-1.2-OH, respectively. In all cases, H_2O content ranges from ~14.0 to ~11.0 mmol/g of dry clay over this domain (Figure 1),[50] and the 2W-to-1W transition spreads over ~10–15% RH. For higher layer charges (from 1.4 to 2.0 per $O_{20}(OH)_4$), this transition initiates also at ~45% RH, with H_2O contents similar to those of lower charge saponites, except for Sap-2.0-OH that exhibits slightly lower interlayer H_2O contents. 1W stability domains thus extend from ~50, 40, or 35% RH (Sap-0.8-OH, Sap-1.0-OH, and higher charge hydroxylated samples, respectively) to ~5% RH (Figure 1). Minimum H_2O contents for 1W samples decrease slightly with decreasing layer charge, from Sap-1.2-OH to Sap-0.8-OH (~4.1 and ~2.6 mmol·g^{-1}, respectively). As for 2W layers, Sap-2.0-OH exhibits slightly lower interlayer H_2O contents than Sap-1.2-OH and Sap-1.4-OH (Figure 1).

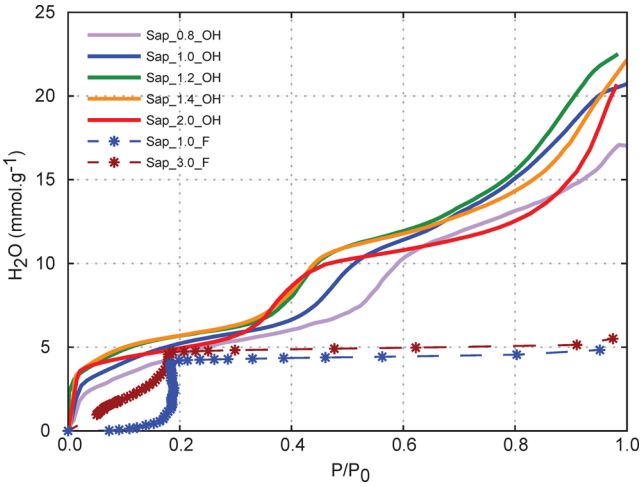

Figure 1. Water content as a function of relative humidity for saponite samples along the water vapor desorption isotherm. Solid and dashed lines indicate OH and F saponites, respectively, whereas the layer charge deficit is color-coded, with purple, blue, green, orange, red, and brown lines corresponding to 0.8, 1.0, 1.2, 1.4, 2.0, and 3.0 charges per $O_{20}(OH,F)_4$. Sap-0.8-OH, Sap-1.0-OH, Sap-1.2-OH, and Sap-1.4-OH isotherms from Ferrage et al.[53]

Contrastingly, the two fluorinated samples present a unique plateau indicative of a stable 1W state over most of the RH range investigated. H_2O content is about constant on this plateau (~4.8–4.2 and ~5.5–4.7 mmol·g^{-1} for Sap-1.0-F and Sap-3.0-F, respectively). The 1W-to-0W transition is complete over a 5% RH range for Sap-1.0-F, while Sap-3.0-F exhibits a smoother transition over a 15% RH span.

XRD Profile Modeling. XRD data and their optimum fits are shown as a function of relative humidity in Figure 2 for hydroxylated samples and in Figure 3 for fluorinated ones. The relative contributions of the mixed layers to the diffracted intensity and their compositions (proportion of the different layer types) are reported in Tables 1–4. These tables report also the main structural parameters of crystals (N), layers (layer-to-layer distance and its fluctuation, σz), and interlayer species content and organization, with Δd parameters for 2W and 1W layers. Compared to previous studies investigating in detail the evolution of smectite hydration along H_2O (de)sorption isotherms,[50,52,88,89] the present study focuses on the impact of smectite crystal chemistry on its hydration. As a consequence, the number of XRD patterns fitted along desorption isotherms has been limited and mainly restricted to those displaying homogeneous hydration states to ease

DOI: 10.1021/jp5123322
J. Phys. Chem. C 2015, 119, 4158–4172

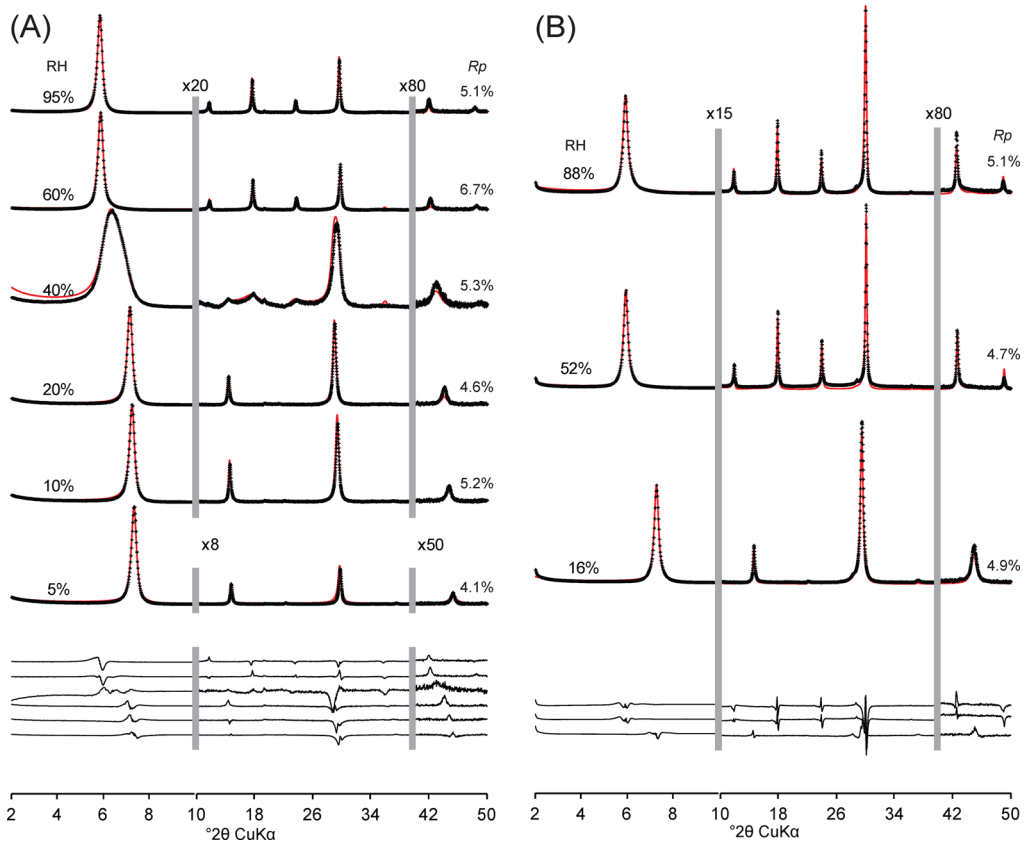

Figure 2. Comparison between experimental and calculated XRD patterns for (A) Sap-1.2-OH and (B) Sap-2.0-OH. Experimental and calculated XRD patterns are shown as crosses and solid lines, respectively. Difference plots are shown at the bottom of the figure. The vertical gray bars indicate a modified scale factor for high-angle regions compared to the 2−10° 2θ angular range. The goodness of fit parameter R_p is indicated for each pattern.

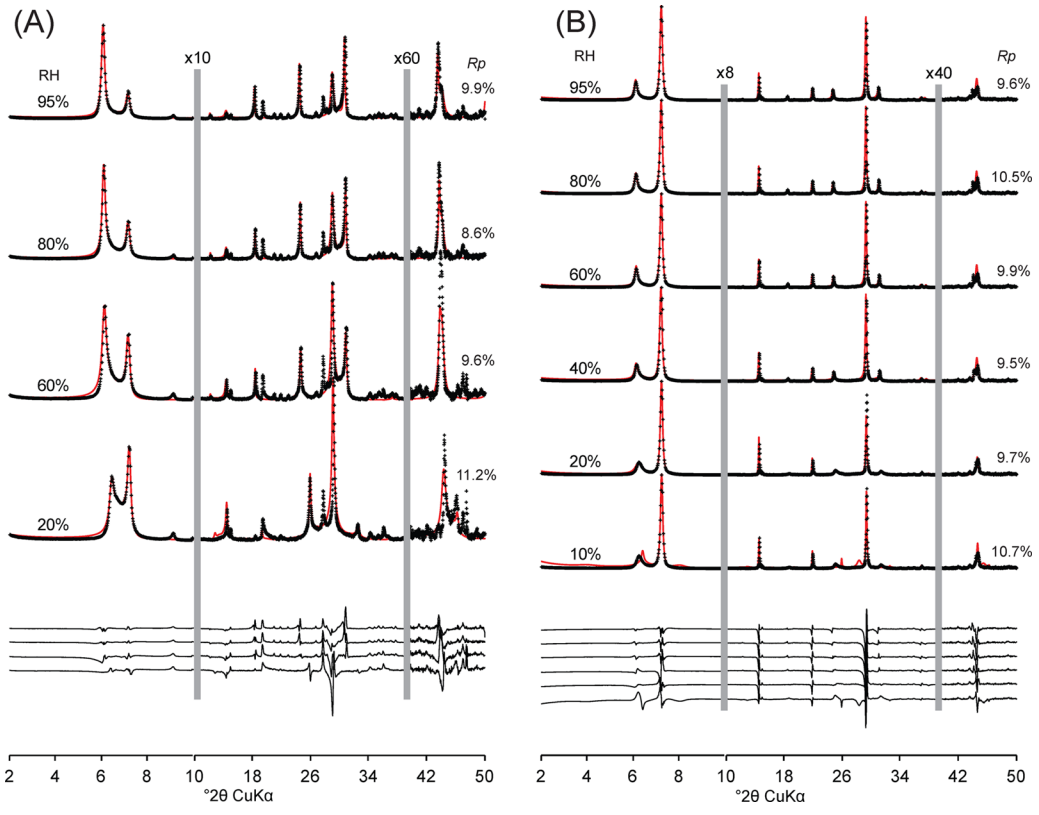

Figure 3. Comparison between experimental and calculated XRD patterns for (A) Sap-1.0-F and (B) Sap-3.0-F. Patterns as for Figure 2.

DOI: 10.1021/jp5123322
J. Phys. Chem. C 2015, 119, 4158−4172

determination of meaningful parameters describing interlayer species content and organization.

Sap-1.2-OH. The XRD pattern recorded at 95% RH was fitted with one periodic 2W smectite with d_{001} = 15.07 Å. At ∼60% RH, a mixed layer containing 2W and 1W layers in similar proportions is needed to account for the high-angle asymmetry of the 001 reflection, but the periodic 2W smectite still represents >90% of the sample before the onset of the 2W-to-1W transition (Figure 2A, Table 1). At 40% RH, three mixed layers are required to fit XRD data, the broad 001 reflection being typical of hydration heterogeneity in transition domains. The initially periodic 2W phase includes 40% of 1W layers, and its contribution is strongly decreased; the 1W content in the initial mixed layer increases from 50 to 70%. Its contribution is also strongly increased (∼40%) in this transition domain. An almost periodic 1W smectite (90% of 1W layers interstratified with 2W ones) allows fitting the broad 001 and 004 reflections and the peak at ∼6.2 Å. At 20 and 10% RH, the transition is complete: none of the contributions is dominated by 2W layers, and a periodic 1W smectite dominates the sample. A minor mixed layer containing 20% of 2W layers accounts for the low-angle broadening of the 001 reflection. Smectite dehydration is initiated at 5% RH, with the presence of a mixed layer containing 30% of 0W layers (d_{001} = 9.70 Å) together with 1W layers. A periodic 1W smectite, with a minimal layer-to-layer distance (d_{001} = 12.02 Å), still dominates the sample, however.

Sap-2.0-OH. Only three XRD patterns were fitted along the H_2O desorption isotherm owing to the very limited evolution of experimental profiles. From ∼90 to ∼50% RH, Sap-2.0-OH is dominated by a periodic 2W smectite, responsible for the rational series of basal reflections. Three additional mixed layers are needed to fit the high-angle asymmetry of the 001 peak, however (Figure 2B, Table 2). The first one accounts for hydration heterogeneity with the coexistence of 2W and 1W layers (70:30 ratio), whereas the second one is an almost periodic 1W smectite (10% 2W layers). A third contribution includes both 1W and 0W layers (55:45 ratio). At 16% RH the 2W-to-1W transition is achieved, and Sap-2.0-OH is dominated (85%) by a periodic 1W smectite accounting for the rational series of basal reflections. Three minor mixed layers are needed to account for various asymmetries. The most abundant one (10%) includes both 1W and 0W layers (78:22 ratio), whereas another mixed layer still contains a minor amount of 2W layers (19%). Finally, a mixed layer containing 1W and 0W (40:60 ratio) is present as in patterns recorded at higher RH conditions.

Sap-1.0-F. From near saturated conditions down to ∼20% RH, XRD patterns of Sap-1.0-F exhibit two almost rational series of reflections corresponding to 2W and 1W smectite. Accordingly, two almost periodic phases were used over this whole RH range to fit XRD data (Figure 3A, Table 3). The 2W smectite contains minor amounts of 0W layers (2−4%), whereas the 1W smectite contains minor amounts of both 2W and 0W layers (2−3% in both cases). The relative contribution of 1W smectite is about stable over the 95−20% RH domain (33−35%), whereas that of the 2W smectite is steadily decreasing from 46% to 15% along the desorption isotherm. Two mixed layer contributions, both including 2W and 1W layers, complete the description of XRD data. The composition of the mixed layer dominated by 2W layers is about stable over the 95−20% RH domain with 70−60% of 2W layers (60% at 20% RH, 70% for other RH conditions). Except for near-saturated conditions where this contribution is minor (6%), this mixed layer accounts for a stable 21−22% of the sample.

Table 3. Structural Parameters Used to Fit Experimental XRD Patterns of Sap-1.0-F as a Function of Relative Humidity

relative humidity %		20	60	80	95
phase 1	ab. (%)	0.15	0.26	0.33	0.46
	0W	0.04	0.04	0.02	0.02
	1W				
	2W	0.96	0.96	0.98	0.98
	CSD size	32	36	36	31
phase 2	ab. (%)	0.35	0.35	0.33	0.34
	0W	0.02	0.02	0.02	0.03
	1W	0.98	0.96	0.96	0.94
	2W		0.02	0.02	0.03
	CSD size	40	40	40	40
phase 3	ab. (%)	0.28	0.18	0.13	0.14
	0W				
	1W	0.85	0.80	0.80	0.70
	2W	0.15	0.20	0.20	0.30
	CSD size	10	10	10	7
phase 4	ab. (%)	0.22	0.21	0.21	0.06
	0W				
	1W	0.40	0.30	0.30	0.30
	2W	0.60	0.70	0.70	0.70
	CSD size	10	8	8	8
number of H_2O molecules per $O_{20}F_4$	1W	3.1	3.3	3.3	3.8
	2W	2.8	3.0	3.1	3.3
Debye−Waller factor of interlayer species	BWat1	15	15	15	20
	BWat2	8	8	8	10
	Bcat	5	5	5	5
layer-to-layer distance (Å)	0W	9.70	9.70	9.70	9.70
	1W	12.27	12.32	12.32	12.33
	2W	13.76	14.48	14.50	14.57
σz (Å)	0W	0.17	0.12	0.07	0.08
	1W	0.20	0.20	0.20	0.20
	2W	0.17	0.12	0.07	0.08
additional parameters	Δ1W (Å)	0.00	0.00	0.00	0.00
	Δ2W (Å)	0.70	1.20	1.20	1.20
	Δ1Cat (Å)	0.50	0.50	0.50	1.00
	Δ2Cat (Å)	0.80	0.80	0.80	0.80
	σ^* (deg)	0.0	0.0	0.0	0.0

Contrastingly the contribution of the mixed layer dominated by 1W layers steadily increases from 14 to 28% at 95 and 20% RH, respectively. Simultaneously the composition of this mixed layer evolves to include more 1W layers (from 70% at 95% RH to 85% at 20% RH) at the expense of 2W layers.

Sap-3.0-F. Over the whole RH range investigated (95−10% RH), the description of XRD data involves essentially the same contributions as for the previous sample. Two periodic phases were used over this whole RH range to reproduce the rational series of basal reflections corresponding to 2W and 1W smectites (Figure 3B, Table 4). Both composition and relative abundance of these two contributions (10−16% and 68−76% for 2W and 1W smectites, respectively) are essentially stable from 95 to 20% RH, whereas the contribution of 2W smectite vanishes at 10% RH (3%). As for Sap-1.0-F, two additional mixed layer contributions help improve the fit to the data. The first one is dominated by 2W layers (75−80%), and its contribution is about constant (7−11%) over the whole RH range. The composition of the second mixed layer is much more variable as it includes 2W and 1W layers (65:35 ratio) at 95% RH and 1W and 0W layers at lower RH conditions. The 1W:0W layer ratio is stable from 80 to 20%

DOI: 10.1021/jp5123322
J. Phys. Chem. C 2015, 119, 4158−4172

Table 4. Structural Parameters Used to Fit Experimental XRD Patterns of Sap-3.0-F as a Function of Relative Humidity

relative humidity %		10	20	40	60	80	95
phase 1	ab. (%)	0.03	0.15	0.10	0.13	0.13	0.16
	0W						
	1W		0.05				
	2W	1.00	0.95	1.00	1.00	1.00	1.00
	CSD size	30	13	23	23	23	23
phase 2	ab. (%)	0.66	0.68	0.76	0.74	0.74	0.76
	0W						
	1W	1.00	1.00	1.00	1.00	1.00	1.00
	2W						
	CSD size	35	35	33	33	33	33
phase 3	ab. (%)	0.08	0.07	0.11	0.09	0.09	0.08
	0W						
	1W	0.20	0.25	0.23	0.23	0.23	0.20
	2W	0.80	0.75	0.77	0.77	0.77	0.80
	CSD size	7	10	9	9	9	15
phase 4	ab. (%)	0.23	0.10	0.03	0.04	0.04	0.02
	0W	0.55	0.30	0.30	0.30	0.30	
	1W	0.45	0.70	0.70	0.70	0.70	0.35
	2W						0.65
	CSD size	9	12	15	15	15	8
number of H_2O molecules per $O_{20}F_4$	1W	2.4	2.5	2.5	2.6	2.6	2.7
	2W	6.9	7.0	7.3	7.5	7.6	8.0
Debye–Waller factor of interlayer species	BWat1	20	20	10	10	10	10
	BWat2	5	10	20	20	20	20
	Bcat	10	5	5	5	5	5
layer-to-layer distance (Å)	0W	9.80	9.80	9.80	9.80	9.80	9.80
	1W	12.18	12.19	12.20	12.21	12.21	12.21
	2W	13.75	14.23	14.35	14.38	14.41	14.44
σz (in Å)	0W	0.01	0.01	0.10	0.10	0.10	0.15
	1W	0.11	0.11	0.14	0.14	0.14	0.15
	2W	0.01	0.01	0.10	0.10	0.10	0.15
additional parameters	Δ1W (Å)	1.40	1.45	0.95	0.95	0.95	0.95
	Δ2W (Å)	1.00	1.00	1.20	1.20	1.20	1.20
	Δ1WCat (Å)	0.30	0.20	0.00	0.00	0.00	0.00
	Δ2WCat (Å)	0.70	0.90	0.90	0.90	0.90	0.90
	σ^* (deg)	6.0	6.0	3.0	3.0	3.0	3.0

RH (70:30) and decreases at 10% RH (45:55). The relative contribution of this mixed layer remains minor down to 40% RH, before increasing to 10 and 23% at 20 and 10% RH, respectively.

Content and Organization of Interlayer Species. *2W Hydroxylated Saponites.* Modeling of XRD data allows allocating the overall content of interlayer H_2O determined from the H_2O vapor (de)sorption isotherms between the different layer types.[50] As a consequence, all 2W hydroxylated saponites contain from 8.5 to 10.0 H_2O molecules per unit cell, independent of their layer charge deficit (Figure 4A). Despite the similar contents of interlayer H_2O, layer-to-layer distance appears strongly and negatively correlated to the layer charge, with d_{001} values ranging from 14.83 to 14.89 Å and from 15.00 to 15.40 Å, for Sap-2.0-OH and Sap-0.8-OH, respectively. The reduction of the layer-to-layer distance with increasing layer charge is accompanied by a reduction of the achievable range for a given layer charge value over the whole RH range. Both reductions are thought to arise from increased electrostatic layer–cation–layer attraction. As the overall interlayer H_2O content is independent of layer charge, the number of interlayer H_2O molecules per interlayer cation logically decreases with increasing layer charge (Figure 4B), with Sap-0.8-OH, Sap-1.2-OH, Sap-1.4-OH, and Sap-2.0-OH hosting ~11.0–12.0, ~9.0–10.0, ~6.0–7.0, and ~4.0–5.0 H_2O molecules per cation, respectively. With ~6 H_2O molecules for the first hydration shell (1HS) of Na^+ cations,[90−97] Sap-0.8-OH and Sap-1.2-OH are both hosting H_2O molecules that are not directly bound to interlayer cations, whereas most H_2O molecules present in Sap-1.4-OH and Sap-2.0-OH are likely hydrating directly interlayer cations. The increased proportion of H_2O molecules bound to interlayer cations with increasing layer charge is responsible for the observed sharpening of the interlayer electron density distribution derived from XRD modeling (Figure 5).

1W Hydroxylated Saponites. Consistent with the previous results, interlayer H_2O contents in 1W saponites range from 3.0 to 5.0 H_2O molecules per unit cell when 1W layers prevail,[50] independent of layer charge (Figure 4C). No systematic evolution of the layer-to-layer distance is observed however with layer charge, although low values of d_{001} were systematically determined for Sap-2.0-OH (12.12–12.15 Å). For other layer charges, the d_{001} range achievable over the whole RH range is about the same (~12.0–13.0 Å) when taking into account the reduced number of XRD patterns fitted in the present study. When normalized to the number of interlayer cations (Figure 4D), the H_2O content of Sap-0.8-OH ranges from ~8.0 to 3.0 H_2O

DOI: 10.1021/jp5123322
J. Phys. Chem. C 2015, 119, 4158–4172

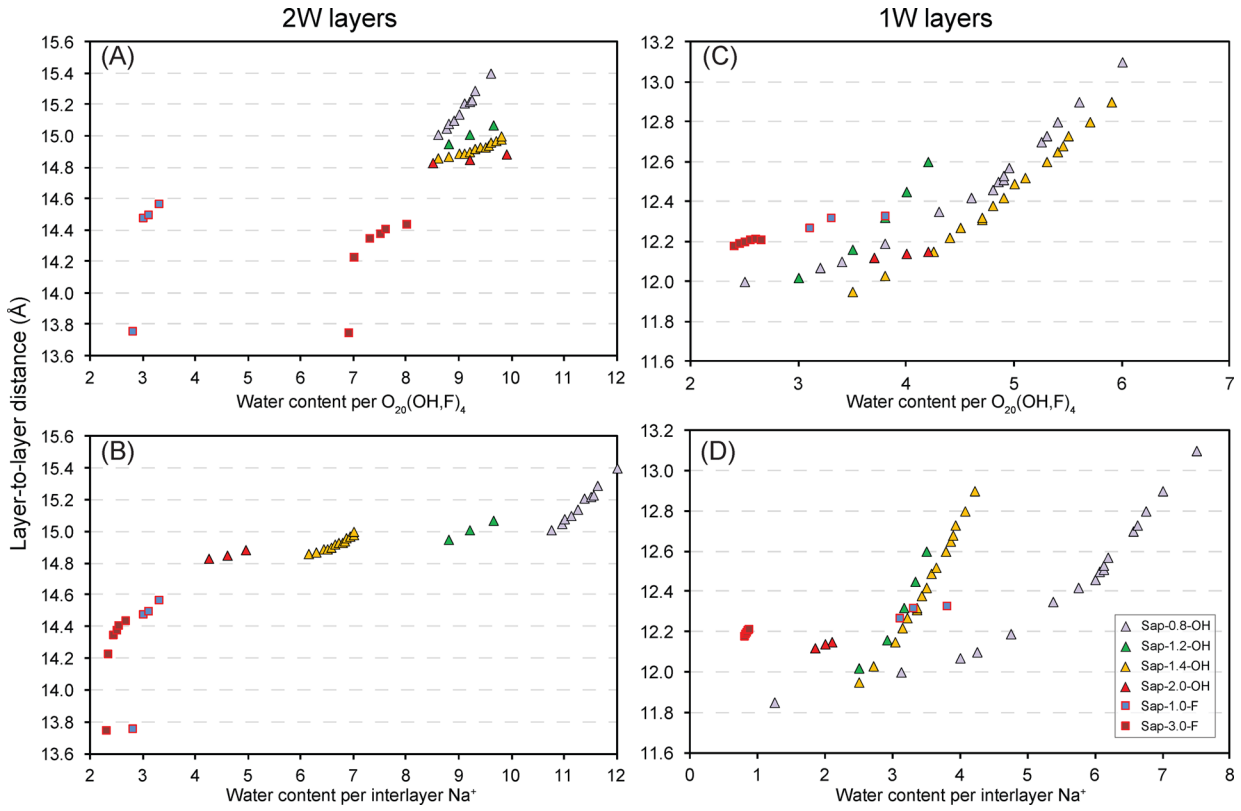

Figure 4. Evolution of the layer-to-layer distance as a function of interlayer water content for (A, B) bi- and (C, D) monohydrated 2W layers. The number of interlayer H_2O molecules is normalized to $O_{20}(OH,F)_4$ (A, C) or to the number of interlayer cations (B, D). Color code as in Figure 1.

molecules with a slope change at ~5.0 H_2O molecules per cation, possibly linked to the H_2O content of the cation 1HS.[50,82] 1W layers of other hydroxylated samples systematically contain less H_2O molecules per cation than this limit (2.0−4.5 H_2O molecule per cation; Figure 4D), and most H_2O molecules are thus likely hydrating directly interlayer cations. Consistent with observations on 2W layers, the increased proportion of H_2O molecules bound to interlayer cations is likely responsible for the observed sharpening of the interlayer electron density distribution with increasing layer charge (Figure 5). In contrast to 2W layers, this sharpening and the induced reduction of layer-to-layer distance do not appear to be steady with increasing layer charge.

Fluorinated Saponites. Consistent with previous reports and with H_2O vapor sorption data,[88] interlayer H_2O content of fluorinated samples is strongly reduced compared to hydroxylated samples of similar charge, 2W layers containing ~6.9−8.0 and ~2.8−3.3 H_2O molecules per unit cell, in Sap-3.0-F and Sap-1.0-F, respectively (Figure 4A), that is ~2.3−3.3 molecules per cation (Figure 4B). Fluorinated samples are thus unlikely hosting H_2O molecules that are not directly bound to interlayer cations. 1W layers of Sap-1.0-F host a similar number of H_2O molecules (3.1−3.8 per unit cell), whereas this number is further reduced for Sap-3.0-F (2.4−2.7 H_2O molecules per cell, that is 0.8−0.9 H_2O molecules per interlayer cation; Figure 4C, 4D). Consistent with the reduced interlayer H_2O content, the layer-to-layer distance is strongly reduced for fluorinated 2W layers and ranges from 13.7 to 14.6 Å. Contrastingly, the layer-to-layer distance of fluorinated 1W layers ranges from 12.2 to 12.3 Å, consistent with their hydroxylated counterparts. This behavior may be accounted for by the specific distribution of interlayer species determined from XRD profile modeling for fluorinated samples. These profiles should be considered globally owing to the weak contrast between Na^+ cations and H_2O molecules when using XRD, both species hosting a similar number of electrons, and to the similar contents of both species in fluorinated samples. For 2W layers, interlayer electron density distributions exhibit two sharp Gaussian peaks and no maximum at the interlayer midplane, in contrast to hydroxylated samples (Figure 5). The sharpness of the two maxima is consistent with the sole presence of H_2O molecules directly bound to interlayer cations. Compared to Sap-1.0-F, interlayer electron density distribution of Sap-3.0-F shows additional shoulders located between the two main maxima and the 2:1 layer. Owing to the hydrophobic nature of the 2:1 layer surface and to the increased layer−cation electrostatic attraction in Sap-3.0-F,[88] these shoulders are likely related to interlayer Na^+ cations forming inner-sphere complexes at the surface of 2:1 layers. Direct, that is, without screening by H_2O molecules, layer−cation electrostatic interactions are likely responsible for the very short layer-to-layer distances determined for 2W layers of fluorinated samples (13.7−14.6 Å; Figure 2). Similar migration of interlayer cations toward the 2:1 layer occurs also in 1W interlayers as evidenced by the two humps on either side of the central maximum of electron density (Sap-3.0-F, Figure 5). In addition, by proscribing short interatomic distances between interlayer H_2O molecules and the 2:1 layer the hydrophobicity of these surfaces is likely responsible for the layer-to-layer distances of 12.2−12.3 Å determined for 1W hydrates despite the very low content of interlayer H_2O.

GCMC Simulations. Over the past few years, molecular simulations of the interlayer space in tetrahedrally charged smectite have achieved a good agreement with experiments, especially for the content and distribution of interlayer

DOI: 10.1021/jp5123322
J. Phys. Chem. C 2015, 119, 4158−4172

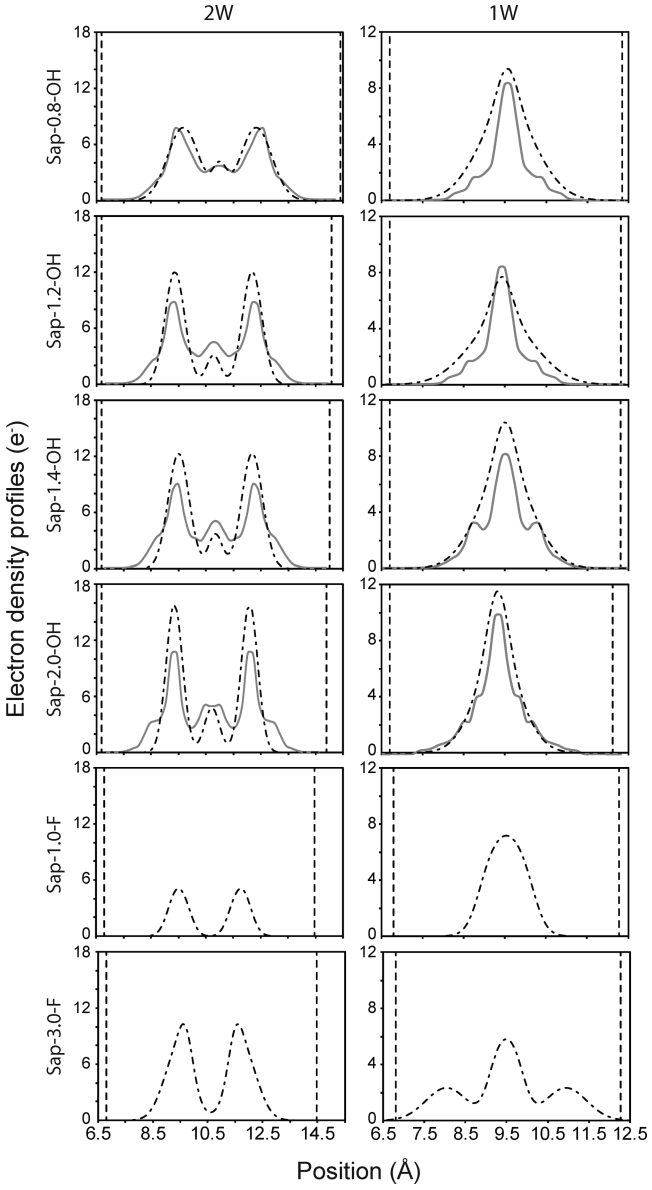

Figure 5. Electronic density profiles within saponite interlayers determined from XRD modeling at ~20 and ~90% RH (1W and 2W interlayers, respectively; dotted dashed lines) and from GCMC calculations (solid gray lines). Dashed lines indicate basal surfaces of the 2:1 layers. Positions are given relative to the basal layer oxygen atoms at the bottom of the 2:1 layer.

species.[50,58,67] It has thus been possible to follow smectite hydration and more especially the evolution of H_2O molecule arrangement along a sorption isotherm.[82] The ability of molecular simulations to account for experimental results can be extended to dynamical processes, allowing differentiating the dynamical behavior of H_2O molecules belonging to interlayer cation hydration sphere and those filling interlayer voids, for example.[27,79] Using appropriate clay and water force fields, it is thus possible to calculate interlayer H_2O contents consistent with water vapor (de)sorption isotherms (Figures 5 and 6) and the distribution of these interlayer species (Figures 5 and 7). The lack of accurate LJ parameters for structural fluorine anions hampers realistic GCMC simulations for equivalent fluorinated systems, however, and the following section will deal only with hydroxylated samples.

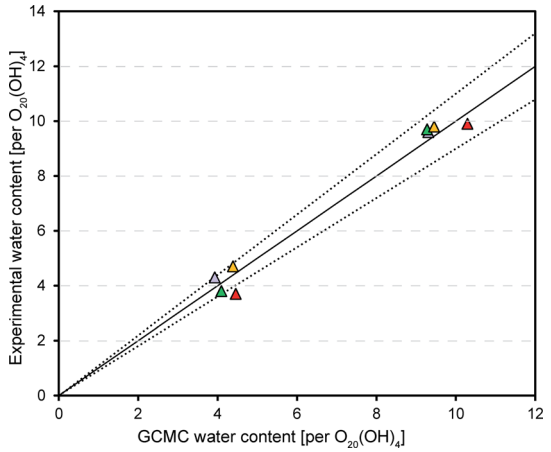

Figure 6. Comparison of the H_2O contents determined from vapor sorption isotherms (and used for XRD modeling) and from GCMC simulations. Solid and dotted lines represent a 1:1 agreement and a ±10% departure from the 1:1 line.

GCMC Interlayer Atomic Density Profiles. Atomic density profiles calculated for the interlayers of 2W saponites (Figure 7) exhibit systematic features. Interlayer cations are mainly present at the interlayer midplane with two additional planes closer to the clay surface, accounting for 14−25% of the overall interlayer cation content. The position of these planes relative to the clay surface is about constant (~2.2−2.3 Å), consistent with Na−O bond lengths, but much larger than proposed previously.[98] In addition, interlayer H_2O molecules are distributed mainly as two main planes corresponding to the two maxima of the oxygen distribution. The distance from each of these planes to the clay surface is about constant (~2.7 Å) independent of the layer charge. The distance from one plane to the other decreases, however, with increasing layer charge to accommodate the reduced layer-to-layer distance determined from XRD (Figure 4A). The contraction of saponite interlayer space induces also a sharpening of the oxygen distribution, consistent with the reduced number of H_2O molecules not directly bound to cations and an increased polarization of H_2O molecules owing to the increased density of undersaturated oxygen atoms at the layer surface. The latter evolution can be estimated from the increased intensity of the hydrogen peaks close to the 2:1 layer surface (Figure 7). To gain further insight into the former evolution, GCMC calculations allow calculating the proportion of H_2O molecules belonging to the cation 1HS (Figure 8) from the radial distribution functions around interlayer cations [$g_{Na-O}(r)$; Figures S1−2, Supporting Information] and considering a maximum Na−H_2O distance of 3.0 Å, consistent with previous studies.[27,58] For Sap-0.8-OH, H_2O molecules from the 1HS represent ~40% of the overall interlayer H_2O content, this proportion steadily increasing to ~70% and 75% for Sap-1.4-OH and Sap-2.0-OH, respectively (Figure 8). A significant change of slope can be observed for a layer charge of ~1.3 e^- per $O_{20}(OH)_4$, matching the smectite−vermiculite charge boundary. A similar trend is observed for 1W layers with a steady increase of the proportion of H_2O molecules from the 1HS from 60%, to ~87%, and further to ~92% for Sap-0.8-Na, Sap-1.4-OH, and Sap-2.0-OH, respectively. A slope change is also observed for a layer charge of ~1.3 e^- per $O_{20}(OH)_4$. It should be noted that this charge also corresponds to the maximum above which the 2W-to-1W transition does not shift to lower RH values (Figure 1). For both 1W and 2W layers, the

DOI: 10.1021/jp5123322
J. Phys. Chem. C 2015, 119, 4158−4172

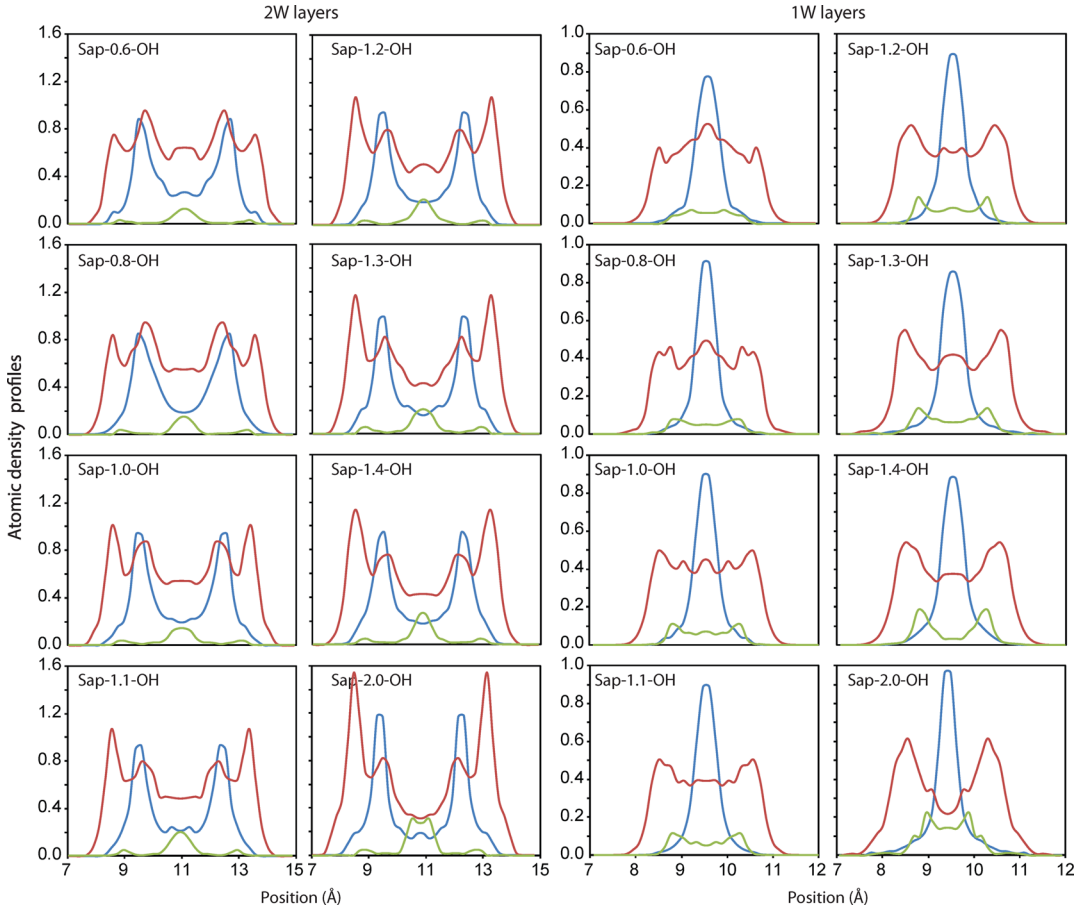

Figure 7. Atomic density profiles for the different interlayer species in mono- and bihydrated states. Profiles for oxygen, hydrogen, and sodium are represented in blue, red, and green, respectively. Atomic densities are given for one of the 40 equivalent divisions of saponite interlayers. Positions are given relative to the basal layer oxygen atoms at the bottom of the 2:1 layer.

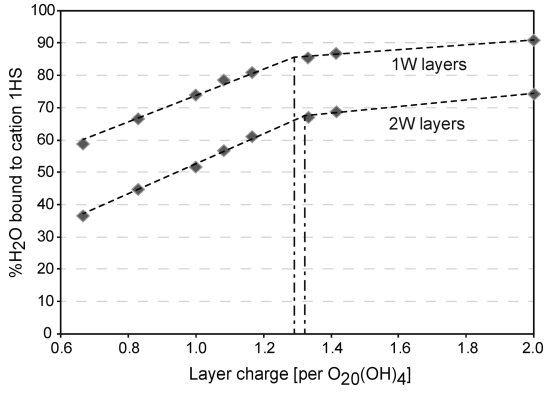

Figure 8. Relative proportion of H_2O molecules belonging to the cations' 1st hydration shell (1HS) as a function of the layer charge. Proportions are determined from GCMC simulations for mono- and bihydrated layers considering a maximum Na–H_2O distance of 3.0 Å (see text for details).

number of H_2O molecules in 1HS is about independent of layer charge at 3.8 and 7.0 molecules per cation, respectively (Figures S1–2, Supporting Information). With increasing layer charge, the distribution of these molecules becomes more regular about Na^+ cations, as shown by the sharper profiles of the $g_{Na-O}(r)$ function (Figures S1–2, Supporting Information). In addition, atomic density profiles calculated for 1W interlayers systematically show a split of the cation distribution on either side of the interlayer midplane. This shift is likely due to tetrahedral substitutions in the 2:1 layer leading to strong undersaturation of layer surface oxygens and decreases with increasing layer charge to accommodate the reduction of the layer-to-layer distance.

*Distribution of Interlayer Cations within the **ab** Plane: Implications for the Smectite–Vermiculite Differentiation.* As the onset of cation ordering within interlayers of expandable phyllosilicates was evoked as a possible limit between smectite and vermiculite,[52] with layer charge ranging from 0.6 to 1.2 and 1.2 to 1.8 per $O_{20}(OH)_4$, respectively, the distribution of these cations was derived also from GCMC simulations. Only 1W interlayers were considered to minimize the impact of cation migration from the interlayer midplane (Figure 7). Neglecting the departure for 1W layers, interlayers of the 6 × 4 unit cells were thus divided according to a Voronoï decomposition centered on interlayer cations.[99−102] In such decomposition, each Voronoï cell contains a unique cation and encompasses the polygonal area closer to this cation than to any other (Figure 9A). For all layer charges, the decomposition was performed on 300 (× 6 × 4 unit cells) thermalized interlayers to achieve representative statistics, and the distribution of Voronoï cell surface areas is plotted in Figure 9B as a box plot to exclude outliers computed for cells close to the simulation box limits. For all layer charges, computed distributions are alike those obtained from a totally random distribution of interlayer cations, calculated over 100 interlayers (× 6 × 4 unit cells) assuming a unique exclusion distance (equal to Na^+ ionic radius)

DOI: 10.1021/jp5123322
J. Phys. Chem. C 2015, 119, 4158–4172

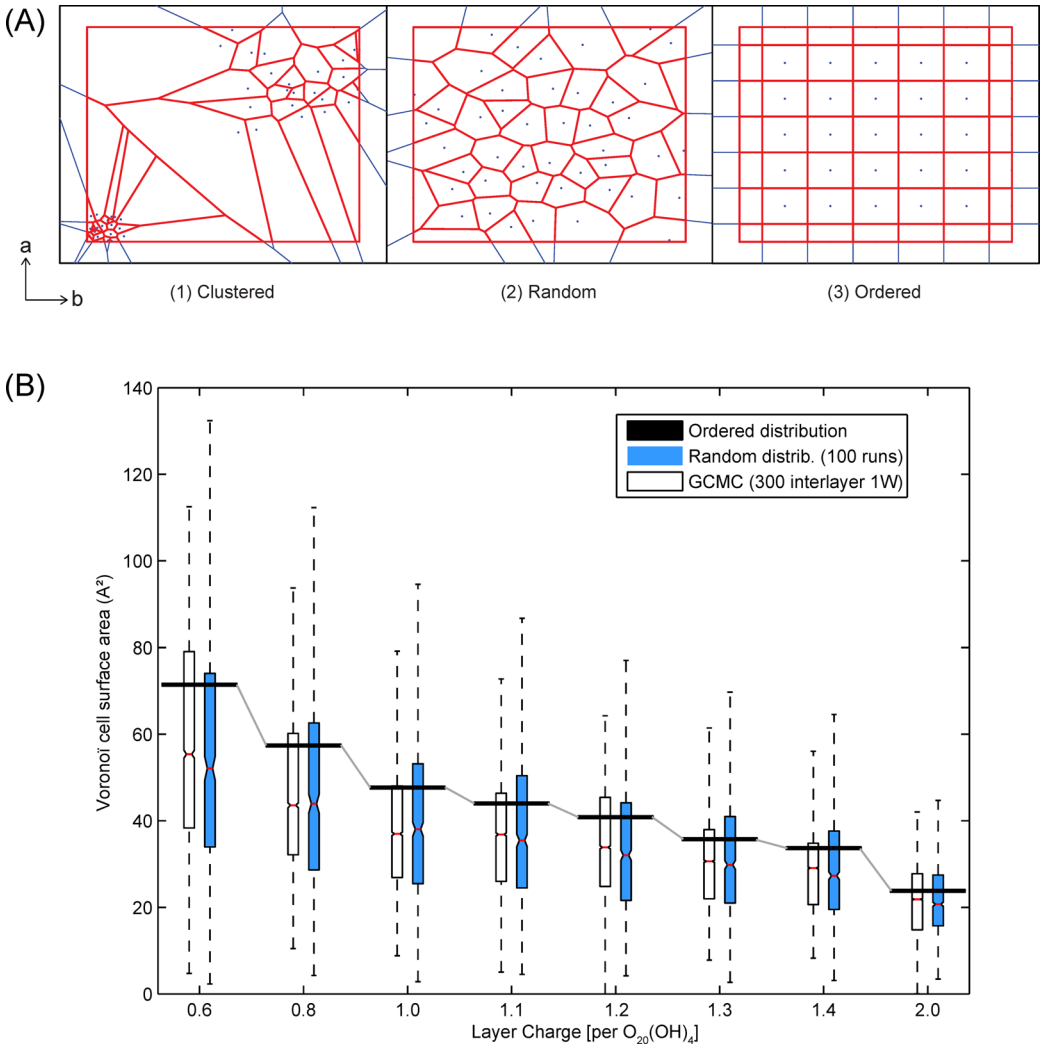

Figure 9. Voronoï distribution of interlayer cations within smectite interlayers. (A) Examples computed for (1) segregated, (2) random, and (3) ordered interlayer cation distributions. (B) Distribution of the Voronoï cell surface area around interlayer cations as a function of layer charge. Distributions are computed within the **ab** plane for 1W saponite interlayers. Results from GCMC simulated (300 interlayers × 6 × 4 unit cells) and from randomly generated (100 interlayers × 6 × 4 unit cells) interlayers are shown as open and blue box plots limited by the 25th below and the 75th above percentile. The red line indicates the median. Upper and lower limits are calculated as the 1.5 × interquartile range above the 75th percentile and below the 25th percentile, respectively. The ordered distribution is computed as the average interlayer surface area occupied by interlayer cations.

around cations to prevent overlaps (Figure 9B). Both GCMC computed and random distributions differ significantly from an ordered distribution of interlayer species, and no increased tendency to ordering is observed with increasing layer charge, in contrast with the hypothesized origin of the smectite-to-vermiculite transition.[50,52] Except for Sap-0.8-OH, the first maximum of computed $g_{Al-Na}(r)$ radial distribution functions (Figure S3A, Supporting Information) accounts for 50% or less of total interlayer Na^+ (Figure S3B, Supporting Information), and distributions of interlayer Na^+ are thus disconnected from those of ^{IV}Al. The absence of interlayer cation ordering is thus likely not induced by the random distribution hypothesized for isomorphic substitutions in smectite tetrahedral sheets. In addition, it should be noted that nuclear magnetic resonance and Ar adsorption data support the hypothesized homogeneous distribution of Al substitutions in saponites, whatever the layer charge.[103−105] Such disordered distribution of Al substitutions was also reported for vermiculite from X-ray scattering investigations of dehydrated samples.[106,107] Upon hydration, the distribution of interlayer Mg and Ni cations becomes ordered, however. Using electron diffraction, ordering of Ba interlayer cations was observed also for 2:1 phyllosilicates with a layer charge deficit higher than 1.2 per $O_{20}(OH)_4$,[108,109] although ordering was not systematically observed for vermiculite.[107] With increasing layer charge, the surface area of Voronoï cells decreases from 40 to 80 $Å^2$ (Sap-0.8-OH) to 18 to 25 $Å^2$ (Sap-2.0-OH). The simultaneous reduction of the range of achievable values occurs, however, steadily without any threshold effect, similar to the steady ordering of H_2O molecules about the cations and consistent with previous reports.[32] The process appears to be driven essentially by the reduction of the interlayer volume, arising from a stronger layer−cation electrostatic attraction and by the increasing amount of interlayer species (cations and a constant number of H_2O molecules for a given hydration state). Both effects lead to the formation of an interlayer cation two-dimensional network, as shown by the presence of several maxima on the $g_{Al-Na}(r)$ functions of Sap-2.0-OH (Figure S3A, Supporting Information). The increased

DOI: 10.1021/jp5123322
J. Phys. Chem. C 2015, 119, 4158−4172

frequency of more than one Al-for-Si substitution per hexagonal ring of six tetrahedra and steric constraints on the distribution of hydrated interlayer cations appear as likely driving factors for network formation. Consistently, minimum steric constraints induce a close interaction between Al-for-Si substitutions and interlayer cations for the lowest charge Sap-0.8-OH, where 80% of interlayer Na^+ are bound to substituted tetrahedra (Figure S3B, Supporting Information).

CONCLUSION

The combined use of XRD profile modeling and of Monte Carlo simulations in the grand canonical ensemble allows drawing a consistent picture of interlayer H_2O and cation organization in tetrahedrally charged smectites. The evolution of this organization as a function of both layer charge and anionic (F-for-OH) isomorphic substitutions can also be deciphered. For a given (1W or 2W) hydration state, H_2O content is about constant in hydroxylated saponites, independent of layer charge. When normalized to the number of interlayer cations, the H_2O content thus decreases with increasing layer charge owing to the reduced number of H_2O molecules not directly bound to the cation first hydration shell. This reduction favors in turn H_2O molecule polarization and minimizes their positional disorder within smectite interlayers. With increasing layer charge, electrostatic attraction between interlayer cations and the 2:1 layer is enhanced, reducing layer-to-layer distance and interlayer thickness and sharpening further the distribution of interlayer H_2O molecules because of stronger steric constraints within interlayers. The increased proportion of H_2O molecules belonging to cation 1HS with increasing layer charge also favors the stability of most hydrated layers toward lower RH values. All trends appear continuous throughout the entire range of layer charge investigated which encompasses the smectite-to-vermiculite transition at ~1.3 e^- charge per $O_{20}(OH)_4$. The stability of most hydrated layers reaches, however, its maximum at this transition, consistent with the slope change in the proportion of H_2O molecules belonging to cation 1HS, for both 1W and 2W hydrates. No onset of cation and/or H_2O molecule ordering is observed at this transition, however. Despite the increased stability of most hydrated layers, the mobility of interlayer H_2O molecules is likely reduced with increasing layer charge owing to their stronger bonding to interlayer cations and to steric constraints.

Similar trends are observed as a function of layer charge for fluorinated smectites. The hydrophobicity of 2:1 layer surfaces is enhanced by F-for-OH substitutions, however, thus reducing dramatically the interlayer H_2O content for fluorinated smectites compared to their hydroxylated counterparts. As a consequence, interlayer cations tend to form inner sphere complexes at the layer surface, enhancing cation–layer electrostatic attraction and thus reducing layer-to-layer distances, compared to hydroxylated smectites of equivalent charge. This reduction is hampered for 1W layers by the hydrophobicity of layer surfaces which precludes short layer–H_2O distances, however.

ASSOCIATED CONTENT

Supporting Information

GCMC computed radial distribution functions and associated distribution of H_2O molecules around interlayer Na^+ cations for 2W and 1W layers with variable charge (Figures S1 and S2, respectively). GCMC computed radial distribution function and associated number of interlayer Na^+ cations adjacent to an Al-for-Si tetrahedral substitution with the relative proportions of cations belonging to the $g(r)$ first neighbor peak (Figure S3–1W layers only). This material is available free of charge via the Internet at http://pubs.acs.org.

AUTHOR INFORMATION

Corresponding Author

*E-mail: baptiste.dazas@ujf-grenoble.fr.

Notes

The authors declare no competing financial interest.

ACKNOWLEDGMENTS

Victor A. Drits is thanked for fruitful discussions on cation ordering, and Nathaniel Findling and Valérie Magnin (ISTerre, Grenoble) are thanked for their assistance during XRD and water vapor isotherm data collection, respectively. The CNRS interdisciplinary défi Needs, through its "MiPor" program, is thanked for the financial support to the present study.

REFERENCES

(1) Berend, I.; Cases, J.-M.; Francois, M.; Uriot, J.-P.; Michot, L.; Masion, A.; Thomas, F. Mechanism of Adsorption and Desorption of Water Vapor by Homoionic Montmorillonites: 2. The Li^+, Na^+, K^+, Rb^+, and Cs^+-Exchanged Forms. *Clays Clay Miner.* **1995**, *43*, 324–336.

(2) Boek, E. S.; Coveney, P. V.; Skipper, N. T. Monte Carlo Molecular Modeling Studies of Hydrated Li-, Na-, and K-Smectites: Understanding the Role of Potassium as a Clay Swelling Inhibitor. *J. Am. Chem. Soc.* **1995**, *117*, 12608–12617.

(3) Cases, J. M.; Berend, I.; Francois, M.; Uriot, J. P.; Michot, L. J.; Thomas, F. Mechanism of Adsorption and Desorption of Water Vapor by Homoionic Montmorillonite: 3. The Mg^{2+}, Ca^{2+}, Sr^{2+} and Ba^{2+} Exchanged Forms. *Clays Clay Miner.* **1997**, *45*, 8–22.

(4) Marry, V.; Turq, P. Microscopic Simulations of Interlayer Structure and Dynamics in Bihydrated Heteroionic Montmorillonites. *J. Phys. Chem. B* **2003**, *107*, 1832–1839.

(5) Young, D. A.; Smith, D. E. Simulations of Clay Mineral Swelling and Hydration: Dependence Upon Interlayer Ion Size and Charge. *J. Phys. Chem. B* **2000**, *104*, 9163–9170.

(6) Sato, T.; Watanabe, T.; Otsuka, R. Effects of Layer Charge, Charge Location, and Energy Change on Expansion Properties of Dioctahedral Smectites. *Clays Clay Miner.* **1992**, *40*, 103–113.

(7) Mooney, R. W.; Keenan, A. G.; Wood, L. A. Adsorption of Water Vapor by Montmorillonite. Ii. Effect of Exchangeable Ions and Lattice Swelling as Measured by X-ray Diffraction. *J. Am. Chem. Soc.* **1952**, *74*, 1371–1374.

(8) Bradley, W. F.; Grim, R. E.; Clark, G. L. A Study of the Behavior of Montmorillonite Upon Wetting. *Z. Kristallogr.* **1937**, *97*, 216–222.

(9) Hendricks, S. B.; Jefferson, M. E. Crystal Structure of Vermiculites and Mixed Vermiculite-Chlorites. *Am. Mineral.* **1938**, *23*, 851–862.

(10) Nagelschmidt, G. On the Lattice Shrinkage and Structure of Montmorillonite. *Z. Kristallogr.* **1936**, *93*, 481–487.

(11) Norrish, K. The Swelling of Montmorillonite. *Discuss. Faraday Soc.* **1954**, *18*, 120–134.

(12) Walker, G. F. The Mechanism of Dehydration of Mg-Vermiculite. *Clays Clay Miner.* **1955**, *4*, 101–115.

(13) Bittelli, M.; Valentino, R.; Salvatorelli, F.; Rossi Pisa, P. Monitoring Soil-Water and Displacement Conditions Leading to Landslide Occurrence in Partially Saturated Clays. *Geomorphology* **2012**, *173–174*, 161–173.

(14) Boullier, A.-M.; Yeh, E.-C.; Boutareaud, S.; Song, S.-R.; Tsai, C.-H. Microscale Anatomy of the 1999 Chi-Chi Earthquake Fault Zone. *Geochem., Geophys., Geosyst.* **2009**, *10*, Q03016.

(15) Boutareaud, S.; Calugaru, D.-G.; Han, R.; Fabbri, O.; Mizoguchi, K.; Tsutsumi, A.; Shimamoto, T. Clay-Clast Aggregates: A New Textural Evidence for Seismic Fault Sliding? *Geophys. Res. Lett.* **2008**, *35*, L05302.

DOI: 10.1021/jp5123322
J. Phys. Chem. C 2015, 119, 4158–4172

(16) Burst, J. F. Diagenesis of Gulf Coast Clayey Sediments and Its Possible Relation to Petroleum Migration. *AAPG Bull.* **1969**, *53*, 73−93.
(17) Matsuda, T.; Omura, K.; Ikeda, R.; Arai, T.; Kobayashi, K.; Shimada, K.; Tanaka, H.; Tomita, T.; Hirano, S. Fracture-Zone Conditions on a Recently Active Fault: Insights from Mineralogical and Geochemical Analyses of the Hirabayashi Nied Drill Core on the Nojima Fault, Southwest Japan, Which Ruptured in the 1995 Kobe Earthquake. *Tectonophysics* **2004**, *378*, 143−163.
(18) Takahashi, A.; Fung, D. W. H.; Jardine, F. In *Swelling Effects on Mechanical Behaviour of Natural London Clay*, Proc. 16th Int. Conf. on Soil Mechanics and Foundation Engineering, 2005; pp 443−446.
(19) Tertre, E.; Ferrage, E.; Bihannic, I.; Michot, L. J.; Prêt, D. Influence of the Ionic Strength and Solid/Solution Ratio on Ca(II)-for-Na^+ Exchange on Montmorillonite. Part 2: Understanding the Effect of the M/V Ratio. Implications for Pore Water Composition and Element Transport in Natural Media. *J. Colloid Interface Sci.* **2011**, *363*, 334−347.
(20) Tertre, E.; Pret, D.; Ferrage, E. Influence of the Ionic Strength and Solid/Solution Ratio on Ca(II)-for-Na^+ Exchange on Montmorillonite. Part 1: Chemical Measurements, Thermodynamic Modeling and Potential Implications for Trace Elements Geochemistry. *J. Colloid Interface Sci.* **2011**, *353*, 248−256.
(21) Vrolijk, P. On the Mechanical Role of Smectite in Subduction Zones. *Geology* **1990**, *18*, 703−707.
(22) Bouma, J.; Jongerius, A.; Boersma, O.; Jager, A.; Schoonderbeek, D. Function of Different Types of Macropores During Saturated Flow Through 4 Swelling Soil Horizons. *Soil Sci. Soc. Am. J.* **1977**, *41*, 945−950.
(23) Malikova, N.; Cadène, A.; Dubois, E.; Marry, V.; Durand-Vidal, S.; Turq, P.; Breu, J.; Longeville, S.; Zanotti, J. M. Water Diffusion in a Synthetic Hectorite Clay Studied by Quasi-Elastic Neutron Scattering. *J. Phys. Chem. C* **2007**, *111*, 17603−17611.
(24) Malikova, N.; Cadène, A.; Marry, V.; Dubois, E.; Turq, P. Diffusion of Water in Clays on the Microscopic Scale: Modeling and Experiment. *J. Phys. Chem. B* **2006**, *110*, 3206−3214.
(25) Malikova, N.; Dubois, E.; Marry, V.; Rotenberg, B.; Turq, P. Dynamics in Clays - Combining Neutron Scattering and Microscopic Simulation. *Z. Phys. Chem.* **2010**, *224*, 153−181.
(26) Marry, V.; Dubois, E.; Malikova, N.; Durand-Vidal, S.; Longeville, S. P.; Breu, J. Water Dynamics in Hectorite Clays: Infuence of Temperature Studied by Coupling Neutron Spin Echo and Molecular Dynamics. *Environ. Sci. Technol.* **2011**, *45*, 2850−2855.
(27) Michot, L. J.; Ferrage, E.; Jimenez-Ruiz, M.; Boehm, M.; Delville, A. Anisotropic Features of Water and Ion Dynamics in Synthetic Na- and Ca-Smectites with Tetrahedral Layer Charge. A Combined Quasi-Elastic Neutron-Scattering and Molecular Dynamics Simulations Study. *J. Phys. Chem. C* **2012**, *116*, 16619−16633.
(28) Barrer, R. M.; Tinker, P. B.; Fowden, L. *Clay Minerals: Their Structure, Behaviour and Use*; Royal Soc.: London, 1984.
(29) Pavlidou, S.; Papaspyrides, C. D. A Review on Polymer−Layered Silicate Nanocomposites. *Prog. Polym. Sci.* **2008**, *33*, 1119−1198.
(30) Sinha Ray, S.; Okamoto, M. Polymer/Layered Silicate Nanocomposites: A Review from Preparation to Processing. *Prog. Polym. Sci.* **2003**, *28*, 1539−1641.
(31) Suquet, H.; Iiyama, J. T.; Kodama, H.; Pezerat, H. Synthesis and Swelling Properties of Saponites with Increasing Layer Charge. *Clays Clay Miner.* **1977**, *25*, 231−242.
(32) Suquet, H.; Pezerat, H. Comments on the Classification of Trioctahedral 2:1 Phyllosilicates. *Clays Clay Miner.* **1988**, *36*, 184−186.
(33) De La Calle, C.; Suquet, H., Vermiculite. In *Hydrous Phyllosilicates: (Exclusive of Micas)*; Bailey, S. W., Ed.; Reviews in Mineralogy 19; Miner. Soc. America: Chantilly, VA, 1988; pp 455−496.
(34) Laird, D. A. Layer Charge Influences on the Hydration of Expandable 2:1 Phyllosilicates. *Clays Clay Miner.* **1999**, *47*, 630−636.
(35) Brindley, G. W.; Pédro, G. *Meeting of the Nomenclature Committee of Aipea*; AIPEA Newsletter: Mexico City, 1976; Vol. *12*, pp 5−6.
(36) Guggenheim, S.; Adams, J. M.; Bain, D. C.; Bergaya, F.; Brigatti, M. F.; Drits, V. A.; Formoso, M. L. L.; Galan, E.; Kogure, T.; Stanjek, H. Summary of Recommendations of Nomenclature Committees Relevant to Clay Mineralogy: Report of the Association Internationale Pour L'etude Des Argiles (AIPEA) Nomenclature Committee for 2006. *Clay Miner.* **2006**, *41*, 863−877.
(37) Méring, J.; Pédro, G. Discussion à Propos des Critères de Classification des Phyllosilicates 2/1. *Bull. Groupe Fr. Argiles* **1969**, *21*, 1−30.
(38) Gates, W. P.; Bouazza, A.; Churchman, G. J. Bentonite Clay Keeps Pollutants at Bay. *Elements* **2009**, *5*, 105−110.
(39) Christidis, G.; Eberl, D. Determination of Layer-Charge Characteristics of Smectites. *Clays Clay Miner.* **2003**, *51*, 644−655.
(40) Dohrmann, R. Cation Exchange Capacity Methodology II: A Modified Silver−Thiourea Method. *Appl. Clay Sci.* **2006**, *34*, 38−46.
(41) Dohrmann, R. Cation Exchange Capacity Methodology I: An Efficient Model for the Detection of Incorrect Cation Exchange Capacity and Exchangeable Cation Results. *Appl. Clay Sci.* **2006**, *34*, 31−37.
(42) Grim, R. E.; Güven, N. *Bentonites — Geology, Mineralogy, Properties and Uses*; Elsevier: New York, 1978.
(43) Kaufhold, S. Comparison of Methods for the Determination of the Layer Charge Density (LCD) of Montmorillonites. *Appl. Clay Sci.* **2006**, *34*, 14−21.
(44) Lagaly, G. Layer Charge Determination by Alkylammonium Ions. In *Layer Charge Characteristics of 2:1 Silicate Clay Minerals*; Mermut, A. R., Ed.; Clay Miner. Soc. Workshop Vol. 6; Clay Miner. Soc.: Chantilly, Va., 1994; Vol. *6*, pp 1−46.
(45) Lagaly, G.; Weiss, A. Determination of the Layer Charge in Mica Type Layer Silicates. In *International Clay Conference*; Heller, L., Ed.; Israel Univ. Press: Jerusalem, Tokyo, Japan, 1969; Vol. *1*, pp 61−80.
(46) Laird, D. A. Evaluation of Structural Formulae and Alkylammonium Methods of Determining Layer Charge. In *Layer Charge Characteristics of 2:1 Silicate Clay Minerals*; Mermut, A. R., Ed.; Clay Miner. Soc. Workshop; Clay Miner. Soc.: Chantilly, Va.; Vol. *6*, pp 79−104.
(47) Newman, A. C. D.; Brown, G., The Chemical Constitution of Clays. In *Chemistry of Clays and Clay Minerals*; Newman, A. C. D., Ed.; John Wiley & sons: New York, 1987; pp 1−128.
(48) Ross, C. S.; Hendricks, S. B. *Minerals of the Montmorillonite Group*; U.S. Geol. Survey Prof. Paper 205-B, 1945; pp 23−79.
(49) Chiou, C. T.; Rutherford, D. W. Effects of Exchanged Cation and Layer Charge on the Sorption of Water and Egme Vapors on Montmorillonite Clays. *Clays Clay Miner.* **1997**, *45*, 867−880.
(50) Ferrage, E.; Lanson, B.; Michot, L. J.; Robert, J.-L. Hydration Properties and Interlayer Organization of Water and Ions in Synthetic Na-Smectite with Tetrahedral Layer Charge. Part 1. Results from X-Ray Diffraction Profile Modeling. *J. Phys. Chem. C* **2010**, *114*, 4515−4526.
(51) Ferrage, E.; Lanson, B.; Sakharov, B. A.; Drits, V. A. Investigation of Smectite Hydration Properties by Modeling Experimental X-Ray Diffraction Patterns: Part I. Montmorillonite Hydration Properties. *Am. Mineral.* **2005**, *90*, 1358−1374.
(52) Ferrage, E.; Lanson, B.; Sakharov, B. A.; Geoffroy, N.; Jacquot, E.; Drits, V. A. Investigation of Dioctahedral Smectite Hydration Properties by Modeling of X-Ray Diffraction Profiles: Influence of Layer Charge and Charge Location. *Am. Mineral.* **2007**, *92*, 1731−1743.
(53) Michot, L. J.; Bihannic, I.; Pelletier, M.; Rinnert, E.; Robert, J.-L. Hydration and Swelling of Synthetic Na-Saponites: Influence of Layer Charge. *Am. Mineral.* **2005**, *90*, 166−172.
(54) Slade, P.; Quirk, J.; Norrish, K. Crystalline Swelling of Smectite Samples in Concentrated NaCl Solutions in Relation to Layer Charge. *Clays Clay Miner.* **1991**, *39*, 234−238.

DOI: 10.1021/jp5123322
J. Phys. Chem. C 2015, 119, 4158−4172

(55) Boek, E. S.; Coveney, P. V.; Skipper, N. T. Molecular Modeling of Clay Hydration: A Study of Hysteresis Loops in the Swelling Curves of Sodium Montmorillonites. *Langmuir* **1995**, *11*, 4629−4631.
(56) Chang, F.-R. C.; Skipper, N. T.; Sposito, G. Computer Simulation of Interlayer Molecular Structure in Sodium Montmorillonite Hydrates. *Langmuir* **1995**, *11*, 2734−2741.
(57) Chang, F.-R. C.; Skipper, N. T.; Sposito, G. Monte Carlo and Molecular Dynamics Simulations of Interfacial Structure in Lithium-Montmorillonite Hydrates. *Langmuir* **1997**, *13*, 2074−2082.
(58) Dazas, B.; Ferrage, E.; Delville, A.; Lanson, B. Interlayer Structure Model of Tri-Hydrated Low-Charge Smectite by X-Ray Diffraction and Monte Carlo Modeling in the Grand Canonical Ensemble. *Am. Mineral.* **2014**, *99*, 1724−1735.
(59) Fu, M. H.; Zhang, Z. Z.; Low, P. F. Changes in the Properties of a Montmorillonite-Water System During the Adsorption and Desorption of Water; Hysteresis. *Clays Clay Miner.* **1990**, *38*, 485−492.
(60) Karaborni, S.; Smit, B.; Heidug, W.; Urai, J.; Oort, E. v. The Swelling of Clays: Molecular Simulations of the Hydration of Montmorillonite. *Science* **1996**, *271*, 1102−1104.
(61) Meleshyn, A.; Bunnenberg, C. Swelling of Na/Mg-Montmorillonites and Hydration of Interlayer Cations: A Monte Carlo Study. *J. Chem. Phys.* **2005**, *123*, 074706−074706−7.
(62) Moore, D. M.; Reynolds, R. C. *X-Ray Diffraction and the Identification and Analysis of Clay Minerals*; Oxford Univ. Press: Oxford, 1997; p 378.
(63) Sakharov, B. A.; Lanson, B. X-Ray Identification of Mixed-Layer Structures. Modelling of Diffraction Effects. In *Handbook of Clay Science*, 2nd ed.; Bergaya, F., Lagaly, G., Eds.; Elsevier: Amsterdam, 2013; Vol. *5B*, pp 51−135.
(64) Skipper, N. T.; Chang, F. R. C.; Sposito, G. Monte-Carlo Simulation of Interlayer Molecular-Structure in Swelling Clay-Minerals 0.1. Methodology. *Clays Clay Miner.* **1995**, *43*, 285−293.
(65) Smith, D. E.; Wang, Y.; Chaturvedi, A.; Whitley, H. D. Molecular Simulations of the Pressure, Temperature, and Chemical Potential Dependencies of Clay Swelling. *J. Phys. Chem. B* **2006**, *110*, 20046−20054.
(66) Zeng, Q. H.; Yu, A. B.; Lu, G. Q.; Standish, R. K. Molecular Dynamics Simulation of the Structural and Dynamic Properties of Dioctadecyldimethyl Ammoniums in Organoclays. *J. Phys. Chem. B* **2004**, *108*, 10025−10033.
(67) Ferrage, E.; Sakharov, B. A.; Michot, L. J.; Delville, A.; Bauer, A.; Lanson, B.; Grangeon, S.; Frapper, G.; Jimenez-Ruiz, M.; Cuello, G. J. Hydration Properties and Interlayer Organization of Water and Ions in Synthetic Na-Smectite with Tetrahedral Layer Charge. Part 2. Toward a Precise Coupling between Molecular Simulations and Diffraction Data. *J. Phys. Chem. C* **2011**, *115*, 1867−1881.
(68) Hamilton, D. L.; Henderson, C. M. B. The Preparation of Silicate Compositions by a Gelling Method. *Mineral. Mag.* **1968**, *36*, 832−838.
(69) Robert, J. L.; Beny, J. M.; Della Ventura, G.; Hardy, M. Fluorine in Micas: Crystal-Chemical Control of the OH-F Distribution Between Trioctahedral and Dioctahedral Sites. *Eur. J. Mineral.* **1993**, *5*, 7−18.
(70) Komarneni, S.; Ravella, R.; Park, M. Swelling Mica-Type Clays: Synthesis by NaCl Melt Method, NMR Characterization and Cation Exchange Selectivity. *J. Mater. Chem.* **2005**, *15*, 4241.
(71) Poirier, J. E.; François, M.; Cases, J. M.; Rouquerol, J. In *Proceedings of the 2nd Engineering Foundation Conference on Fundamentals of Adsorption*; Liapis, A. I., Ed., 1987; pp 473−482.
(72) Drits, V. A.; Sakharov, B. A. *X-ray Structural Analysis of Mixed-Layer Minerals*; Nauka: Moscow, 1976; p 256.
(73) Drits, V. A.; Tchoubar, C. *X-Ray Diffraction by Disordered Lamellar Structures Theory and Applications to Microdivided Silicates and Carbons*; Springer-Verlag: Berlin, 1990; p 371.
(74) Howard, S. A.; Preston, K. D. Profile Fitting of Powder Diffraction Patterns. In *Modern Powder Diffraction*; Bish, D. L.; Post, J. E., Eds.; Reviews in Mineralogy 20; Miner. Soc Amer.: Washington DC, 1989; pp 217−275.
(75) Adams, D. J. Chemical Potential of Hard-Sphere Fluids by Monte Carlo Methods. *Mol. Phys.* **1974**, *28*, 1241−1252.
(76) Adams, D. J. Grand Canonical Ensemble Monte Carlo for a Lennard-Jones Fluid. *Mol. Phys.* **1975**, *29*, 307−311.
(77) Allen, M. P.; Tildesley, D. J. *Computer Simulation of Liquids*; Oxford Univ. Press: New York, 1994; p 412.
(78) Delville, A. Modeling the Clay-Water Interface. *Langmuir* **1991**, *7*, 547−555.
(79) Jiménez-Ruiz, M.; Ferrage, E.; Delville, A.; Michot, L. J. Anisotropy on the Collective Dynamics of Water Confined in Swelling Clay Minerals. *J. Phys. Chem. A* **2012**, *116*, 2379−2387.
(80) Michot, L. J.; Delville, A.; Humbert, B.; Plazanet, M.; Levitz, P. Diffusion of Water in a Synthetic Clay with Tetrahedral Charges by Combined Neutron Time-of-Flight Measurements and Molecular Dynamics Simulations. *J. Phys. Chem. C* **2007**, *111*, 9818−9831.
(81) Porion, P.; Faugère, A. M.; Delville, A. ^{1}H and ^{7}Li NMR Pulsed Gradient Spin Echo Measurements and Multiscale Modeling of the Water and Ionic Mobility within Aqueous Dispersions of Charged Anisotropic Nanoparticles. *J. Phys. Chem. C* **2008**, *112*, 11893−11900.
(82) Rinnert, E.; Carteret, C.; Humbert, B.; Fragneto-Cusani, G.; Ramsay, J. D. F.; Delville, A.; Robert, J.-L.; Bihannic, I.; Pelletier, M.; Michot, L. J. Hydration of a Synthetic Clay with Tetrahedral Charges: A Multidisciplinary Experimental and Numerical Study. *J. Phys. Chem. B* **2005**, *109*, 23745−23759.
(83) Cygan, R. T.; Greathouse, J. A.; Heinz, H.; Kalinichev, A. G. Molecular Models and Simulations of Layered Materials. *J. Mater. Chem.* **2009**, *19*, 2470−2481.
(84) Aaqvist, J. Ion-Water Interaction Potentials Derived from Free Energy Perturbation Simulations. *J. Phys. Chem.* **1990**, *94*, 8021−8024.
(85) Heyes, D. M. Pressure Tensor of Partial-Charge and Point-Dipole Lattices with Bulk and Surface Geometries. *Phys. Rev. B* **1994**, *49*, 755−764.
(86) Rouquerol, F.; Rouquerol, J.; Sing, K. S.; Llewellyn, P.; Maurin, G. *Adsorption by Powders and Porous Solids: Principles, Methodology and Applications*, 2nd ed.; Elsevier: Amsterdam, 2014; p 626.
(87) Sing, K. S. W.; Everett, D. H.; Haul, R. A. W.; Moscou, L.; Pierotti, R. A.; Rouquerol, J.; Siemieniewska, T. Reporting Physisorption Data for Gas/Solid Systems with Special Reference to the Determination of Surface Area and Porosity (Recommendations 1984). *Pure Appl. Chem.* **1985**, *57*, 603−619.
(88) Dazas, B.; Lanson, B.; Breu, J.; Robert, J.-L.; Pelletier, M.; Ferrage, E. Smectite Fluorination and Its Impact on Interlayer Water Content and Structure: A Way to Fine Tune the Hydrophilicity of Clay Surfaces? *Microporous Mesoporous Mater.* **2013**, *181*, 233−247.
(89) Ferrage, E.; Lanson, B.; Malikova, N.; Plançon, A.; Sakharov, B. A.; Drits, V. A. New Insights on the Distribution of Interlayer Water in Bi-Hydrated Smectite from X-Ray Diffraction Profile Modeling of 00l Reflections. *Chem. Mater.* **2005**, *17*, 3499−3512.
(90) Allen, T. W.; Bliznyuk, A.; Rendell, A. P.; Kuyucak, S.; Chung, S. H. The Potassium Channel: Structure, Selectivity and Diffusion. *J. Chem. Phys.* **2000**, *112*, 8191−8204.
(91) Barnett, R. N.; Landman, U. Hydration of Sodium in Water Clusters. *Phys. Rev. Lett.* **1993**, *70*, 1775−1778.
(92) Carrillo-Tripp, M.; Saint-Martin, H.; Ortega-Blake, I. A Comparative Study of the Hydration of Na^+ and K^+ with Refined Polarizable Model Potentials. *J. Chem. Phys.* **2003**, *118*, 7062−7073.
(93) Mahler, J.; Persson, I. A Study of the Hydration of the Alkali Metal Ions in Aqueous Solution. *Inorg. Chem.* **2012**, *51*, 425−438.
(94) Obst, S.; Bradaczek, H. Molecular Dynamics Study of the Structure and Dynamics of the Hydration Shell of Alkaline and Alkaline-Earth Metal Cations. *J. Phys. Chem.* **1996**, *100*, 15677−15687.
(95) Smirnov, P. R.; Trostin, V. N. Structure of the Nearest Surrounding of the Na^+ Ion in Aqueous Solutions of Its Salts. *Russ. J. Gen. Chem.* **2007**, *77*, 844−850.
(96) Titiloye, J. O.; Skipper, N. T. Computer Simulation of the Structure and Dynamics of Methane in Hydrated Na-Smectite Clay. *Chem. Phys. Lett.* **2000**, *329*, 23−28.

DOI: 10.1021/jp5123322
J. Phys. Chem. C 2015, 119, 4158−4172

(97) White, J. A.; Schwegler, E.; Galli, G.; Gygi, F. The Solvation of Na^+ in Water: First-Principles Simulations. *J. Chem. Phys.* **2000**, *113*, 4668−4673.
(98) Ben Brahim, J.; Besson, G.; Tchoubar, C. Etude des Profils des Bandes de Diffraction X d'une Beidellite-Na Hydratée à Deux Couches d'Eau. Détermination du Mode d'Empilement des Feuillets et des Sites Occupés par l'Eau. *J. Appl. Crystallogr.* **1984**, *17*, 179−188.
(99) Icke, V.; van de Weygaert, R. Fragmenting the Universe. *Astron. Astrophys.* **1987**, *184*, 16−32.
(100) Miri, M. F.; Stark, H. The Role of Liquid Films for Light Transport in Dry Foams. *EPL (Europhys. Lett.)* **2004**, *65*, 567.
(101) Van der Burg, M.; Shulmeister, V.; Van der Geissen, E.; Marissen, R. On the Linear Elastic Properties of Regular and Random Open-Cell Foam Models. *J. Cell. Plast.* **1997**, *33*, 31−54.
(102) Zhu, H. X.; Hobdell, J. R.; Windle, A. H. Effects of Cell Irregularity on the Elastic Properties of 2D Voronoi Honeycombs. *J. Mech. Phys. Solids* **2001**, *49*, 857−870.
(103) Sanz, J.; Robert, J.-.L. Influence of Structural Factors on ^{29}Si and ^{27}Al NMR Chemical Shifts of Phyllosilicates 2:1. *Phys. Chem. Miner.* **1992**, *19*, 39−45.
(104) Sanz, J.; Robert, J.-.L.; Diaz, M.; Sobrabos, I. Influence of Charge Location on ^{29}Si NMR Chemical Shifts of 2:1 Phyllosilicates. *Am. Mineral.* **2006**, *91*, 544−550.
(105) Michot, L. J.; Villiéras, F. Assessment of Surface Energetic Heterogeneity of Synthetic Na-Saponites. The Role of Layer Charge. *Clay Miner.* **2002**, *37*, 39−57.
(106) Alcover, J. F.; Gatineau, L. Mérıng, Exchangeable Cation Distribution in Nickel- and Magnesium-Vermiculites. *Clays Clay Miner.* **1973**, *21*, 131−136.
(107) Drits, V. A. *Electron Diffraction and High-Resolution Electron Microscopy of Mineral Structures*; Springer-Verlag: Berlin, 1987; p 304.
(108) Besson, G.; Tchoubar, C.; Mering, J. Phénomènes de Diffraction Produits par les Systèmes Stratifiés à Distribution d'Atomes Partiellement Différente de Couche à Couche. *J. Appl. Crystallogr.* **1974**, *7*, 345−350.
(109) Besson, G.; Mifsud, A.; Tchoubar, C.; Mering, J. Order and Disorder in the Distribution Of The Substitutions in Smectites, Illites, and Vermiculites. *Clays Clay Miner.* **1974**, *22*, 379−384.

DOI: 10.1021/jp5123322
J. Phys. Chem. C 2015, 119, 4158−4172